

5R.5 THE POTENTIAL FOR WATER VAPOR AND PRECIPITATION ESTIMATION WITH A DIFFERENTIAL-FREQUENCY RADAR

Robert Meneghini¹, Liang Liao² and Lin Tian³

¹Code 614.6, NASA/GSFC, Greenbelt, MD 20771

²Goddard Earth Science and Technology Center/ Caelum Research Corp., Rockville, MD 20850

³Goddard Earth Science and Technology Center/ University of MD, Baltimore, MD

1. INTRODUCTION

Despite the importance of measuring water vapor in the presence of precipitation, the measurement is a difficult one. Nevertheless, progress has been made recently for ground-based measurements using multi-channel radiometers [Liljegren, 2004; Ware et al., 2004]. Progress also has been recently reported using data from a dual-wavelength airborne Doppler radar [Tian et al., 2004]. In the present paper we analyze the feasibility of such estimates using simulations of the radar return powers from a three-frequency radar, with center frequency at 22.235 GHz and upper and lower frequencies on either side of the line center. A linear combination of differential measurements between the center and lower frequencies on one hand and the upper and lower frequencies on the other provide an estimate of differential water vapor absorption. Cross-talk or interference between the precipitation and water vapor estimates depends on the frequency separation of the channels as well as on the phase state and the median mass diameter of the hydrometeors. Simulations of the retrieval of water vapor absorption show that the largest source of variability arises from the variance in the measured radar return powers while the largest biases occur in the mixed-phase region. Measurements over a fractional bandwidth, defined as the ratio of the difference between the upper and lower frequencies to the center frequency, up to about 0.2 should be possible in a differential frequency mode, where a single transceiver and antenna are used. Restrictions in frequency allocation may require alternative choices of frequency where the water vapor absorptions at the low and high frequencies are not equal. We consider the degradation in the retrieval accuracy when the frequencies are not optimum.

2. EQUATIONS FOR WATER VAPOR ABSORPTION

It is instructive to examine the graphs in Fig. 1, top, showing the specific absorption (dB/km) of water vapor versus frequency for three water vapor densities using the model of Waters (1976) and Ulaby et al. (1981). Also shown are the specific attenuation of rain, using the Marshall-Palmer DSD, for 3 rain rates. As in previous work [Meneghini et al., 2005] the center frequency, f_c , is

chosen at the line center, 22.235 GHz and the upper, f_u , and lower frequency, f_l , are chosen such that $f_l < f_c < f_u$. In contrast to the previous work, however, the assumption of equal water vapor absorption at the lower and higher frequencies, $k_v(f_l) = k_v(f_u)$, is no longer a requirement.

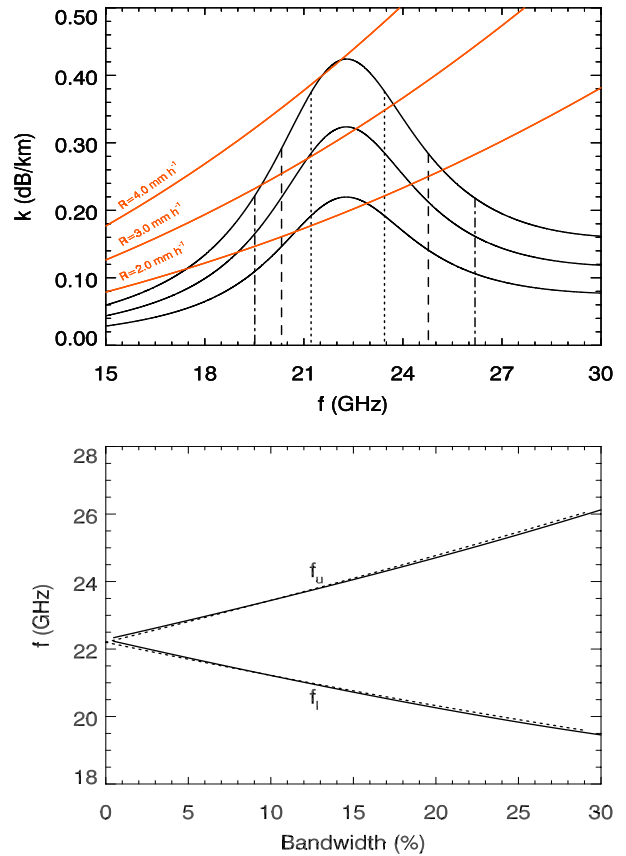


Fig. 1. Top: Water vapor absorption versus frequency for water vapor densities (g/m^3) of 8.75 (bottom), 13.15, 17.5 (top) (black solid lines); vertical lines indicate frequencies for which the fractional bandwidth, defined by $(f_u - f_l)/f_c$, is 0.1 (dotted), 0.2 (dashed) and 0.3 (dashed-dot); red lines show frequency dependence of rain attenuation for the MP distribution for rain rates of 2, 3, 4 mm/h. Bottom: Upper and lower frequencies for which $k_v(f_u) = k_v(f_l)$ versus fractional bandwidth ($\times 100$); dotted lines represent quadratic approximations.

Corresponding author address: Robert Meneghini, Code 614.6, NASA/GSFC, Greenbelt, MD 20771, email: bob@neptune.gsfc.nasa.gov

Let $\tilde{Z}_m(r, f)$ denote $10 \log_{10} Z_m$, where Z_m is the measured radar reflectivity factor. Since this quantity is directly proportional to the radar return power, we consider it a measurable quantity. In the presence of attenuation, \tilde{Z}_m , can be related to the effective radar reflectivity factor in dB, \tilde{Z} , by

$$\tilde{Z}_m(r, f) = \tilde{Z}(r, f) - c \int_0^r (k_p + k_c + k_v) ds \quad (1)$$

where k_p, k_c, k_v are, respectively, the specific attenuations from precipitation, cloud water and water vapor; assuming that these are given in units of dB/km, then $c = 2$. We also employ the following notation for the two-way differential path attenuation from precipitation and cloud and for the differential water vapor absorption ($f_i > f_j$):

$$A_{pc}(f_i, f_j) = 2 \int_0^r [(k_p(f_i) + k_c(f_i)) - (k_p(f_j) + k_c(f_j))] ds \quad (2)$$

$$A_v(f_i, f_j) = 2 \int_0^r [k_v(f_i) - k_v(f_j)] ds \quad (3)$$

The difference in measured reflectivity factors (dB) between the upper and lower frequencies and the center and lower frequencies can be written respectively as:

$$\tilde{Z}_m(f_u) - \tilde{Z}_m(f_l) = \tilde{Z}(f_u) - \tilde{Z}(f_l) - [A_{pc}(f_u, f_l) + A_v(f_u, f_l)] \quad (4)$$

$$\tilde{Z}_m(f_c) - \tilde{Z}_m(f_l) = \tilde{Z}(f_c) - \tilde{Z}(f_l) - [A_{pc}(f_c, f_l) + A_v(f_c, f_l)] \quad (5)$$

To eliminate A_{pc} from the equations, we assume that the differential attenuation from cloud and precipitation between (f_c, f_l) can be expressed as a fraction γ of the differential attenuation from cloud and precipitation between (f_u, f_l); i.e.,

$$A_{pc}(f_c, f_l) = \gamma A_{pc}(f_u, f_l) \quad (6)$$

In the case of Rayleigh scattering, the frequency dependence of k_p, k_c is $f \text{Im}(-K(f))$ where $K = (m^2 - 1)/(m^2 + 2)$ where m is the complex index of refraction of the scatterers so that

$$\gamma = \frac{f_c \text{Im}(-K(f_c)) - f_l \text{Im}(-K(f_l))}{f_u \text{Im}(-K(f_u)) - f_l \text{Im}(-K(f_l))} \quad (7)$$

For liquid water, the above approximation is relatively insensitive to temperature changes: for example, for a fractional bandwidth, $(f_u - f_l)/f_c$, of 0.2, γ changes by less than 1% as the temperature varies from 0 C to 30 C. Nevertheless, because of non-Rayleigh scattering of the hydrometeors, the effects of attenuation from cloud and precipitation can not be eliminated over the entire path for any single value of γ .

Multiplying (4) by γ and subtracting the resulting equation from (5) gives:

$$2 \int_0^r [k_v(f_c) - (1 - \gamma)k_v(f_l) - \gamma k_v(f_u)] ds = G_m(\gamma) - (E_1 + E_2) \quad (8)$$

where

$$G_m(\gamma) = \gamma \tilde{Z}_m(f_u) + (1 - \gamma) \tilde{Z}_m(f_l) - \tilde{Z}_m(f_c) \quad (9)$$

$$E_1 = G(\gamma) = \gamma \tilde{Z}(f_u) + (1 - \gamma) \tilde{Z}(f_l) - \tilde{Z}(f_c) \quad (10)$$

$$E_2 = A_{pc}(f_c, f_l) - \gamma A_{pc}(f_u, f_l) \quad (11)$$

Note that E_2 represents the error in the assumption given by (6). Both bias terms, E_1, E_2 , are approximately zero when the scattering from the hydrometeors is Rayleigh. G_m is a function of the parameter γ and the measured reflectivity factors at the 3 frequencies and serves as an estimate for the left-hand side of (8). If the upper and lower frequencies are chosen such that $k_v(f_l) = k_v(f_u)$ then the left-hand side of (8) reduces to $2 \int_0^r [k_v(f_c) - k_v(f_l)] ds$, the differential water vapor absorption to range r between frequencies (f_c, f_l).

If the water vapor absorption is written as:

$$k_v(f) = \rho_v \xi(f, T, P) / 2 \quad (12)$$

where ρ_v is the water vapor density (g/m^3) and T and P denote temperature and pressure, then, assuming that the bias terms in (8) are zero, an estimate of ρ_v can be obtained by substituting (12) into (8) and differentiating with respect to range:

$$\rho_v = W^{-1} \frac{d}{dr} G_m(\gamma) \quad (13)$$

where

$$W = \xi(f_c) - (1-\gamma)\xi(f_l) - \gamma\xi(f_c) \quad (14)$$

Although (13) is conceptually useful, the estimation of ρ_v from (13) is numerically unstable. It is desirable, moreover, to use a more accurate approximation than (12) where ρ_v and $k_v(f)$ are non-linearly related. For the results shown later, ρ_v is estimated from the discrete form of (8) with the bias terms set to zero using the $k_v(f) - \rho_v$ relationship obtained from the Waters' model.

3. SIMULATION RESULTS

To simulate the precipitation, cloud water, and water vapor, we begin with 1539 drop size distributions measured by an impact disdrometer at Wallops Flight Facility in Sept. 2001. Corresponding to each DSD, a vertical column of precipitation is constructed consisting of a layer of snow from 4-5 km above the surface, a melting layer below this, followed by a rain layer down to the surface. The bottom panel of Fig. 2 shows the median mass diameter of the raindrop size distribution; in the snow and melting layer the size distribution is modified so that the equivalent rain rate is constant along each column. The shape parameter or μ value of the gamma size distribution is assumed to be fixed at 2. For the examples shown, the snow density is taken to be 0.2 g/cm^3 ; the Yokoyama and Tanaka melting model and the effective medium approximation provide the fractional melt water and scattering properties of the mixed phase particles. A 1-km layer of cloud liquid water of 1 g m^{-3} about the melting layer gives a vertically-integrated cloud water content of 1 kg m^{-2} . The relative humidity is assumed to be 100% in the region from 4 to 5 km, decreasing linearly to 70% at the surface. The temperature lapse rate is taken to be 6° km^{-1} giving a surface temperature is 24 C. Although the relative humidity is fixed, the temperature and pressure are assumed to have small variations about their mean values so that the height profile of the water vapor density profiles vary slightly with sequence number.

In the top panel of Fig., 2 simulated height profiles of $\tilde{Z}_m(22.235)$ are shown from a nadir-viewing radar above the precipitation. Evidence of attenuation and a bright-band are apparent. The middle panel shows range profiles of differential effective reflectivity factors between the high and low frequencies. This quantity is independent of the particle concentration; moreover, as $k_v(f_l) \approx k_v(f_u)$ in this case, the quantity is approximately independent of water vapor absorption.

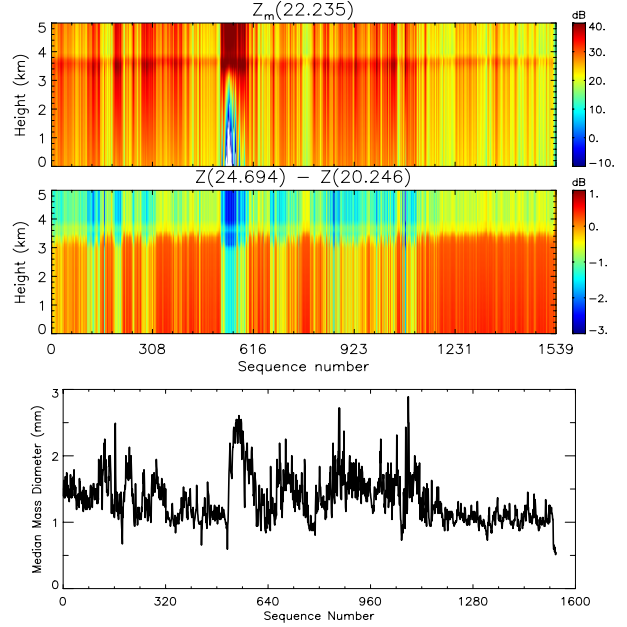


Fig. 2. Top: simulated data for $\tilde{Z}_m(22.235)$ for 1539 range profiles; Center: simulated data for the differential radar reflectivity factors at 24.694 and 20.246 GHz; Bottom: Disdrometer-measured values of D_0 .

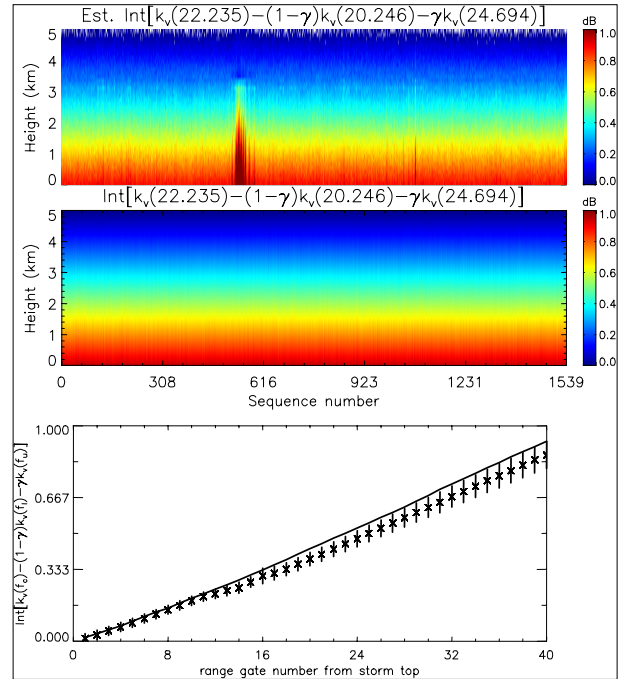


Fig. 3. Top: $G_m(\gamma)$ as estimate of the LHS of (8); Center: True value of differential-frequency water vapor absorption, given by the LHS of (8); Bottom: True value of LHS of (8) (solid line) and mean (X) of estimate versus range. Twice the standard deviation of the estimate is represented by the length of the vertical bar.

Using (7) and the above frequencies, we obtain $\gamma=0.425$; $G_m(\gamma)$ is then computed from (9) and provides an estimate for the left-hand side of (8). Results of the retrieval are shown in the top and bottom panels of Fig. 3. Comparisons of the estimated (top) and assumed or true values (middle panel) of the differential water vapor absorption show that while the estimated profiles are generally accurate, there are several sources of error. An obvious difference appears in the region between sequence numbers 518 and 590 where the estimated water vapor absorption is much larger than the true value. This discrepancy is caused by the high values of D_0 and rain rate in this region, with values of the latter quantity approaching 100 mm/h. Another source of error arises from the sampling error in the measured radar reflectivity factors. Although we have assumed that the estimates are obtained from a large number of independent samples (64,000), variations in $G_m(\gamma)$ are still evident in the fine-scale variability seen in results in the top panel of Fig. 3. The height profiles of the true (solid line) and estimated mean (X) differential vapor absorption are shown in the bottom panel where twice the standard deviation of the estimate is given by the length of the vertical bars.

To investigate the error sources in more detail, we plot in Fig. 4 the E_1, E_2 error terms from (10) and (11) versus the median mass diameter, D_0 . In the graphs of E_1 (top panel), it can be seen that the error depends on the phase state of the hydrometeors: in the snow, E_1 is small; in rain, it is negatively biased; while for the two gates shown in the melting layer, E_1 is negative for small D_0 and positive for large D_0 . It is also of interest to note that for a given hydrometeor type, E_1 is determined by D_0 and is nearly independent of the particle number concentration. The E_2 error, shown in the bottom panel of Fig. 4, differs from E_1 in several respects: for D_0 less than about 2 mm, the E_2 error is small for all hydrometeor types; beyond 2 mm, the error increases rapidly and tends to be positive in rain and negative in snow. Unlike the E_1 error, E_2 also depends on number concentration which accounts for the fact that multiple values of E_2 exist (corresponding to different N_T values) for the same D_0 .

As indicated by (13), the estimate of the range-profiled water vapor density proceeds by calculating the range derivative of the estimated differential path absorption in the form of a linear combination of measured reflectivity factors. Because the variability in the estimated differential path absorption is large relative to its magnitude, range averaging is needed to reduce the error in much the same way that averaging is needed to estimate κ_{dp} from ϕ_{dp} in polarimetric radar retrievals. For the results shown in Figs. 5 and 6, we have used a 5-gate (125-m gates) running average, followed by a differencing over successive 5-gate intervals. After normalizing by the range difference, the procedure provides an estimate of the integrand of the LHS of (8). The mean and standard deviation of the range profile

are shown in the top and bottom right-hand panels of Fig. 5. From the estimate of the differential specific attenuation and model temperature and pressure

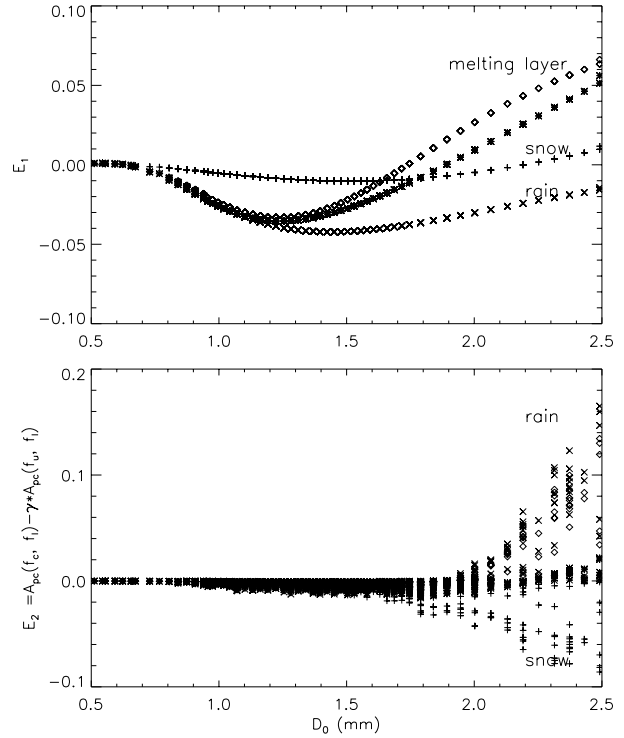


Fig. 4. E_1 (top) and E_2 (bottom) versus D_0 for range gates in the snow, rain and melting layer.

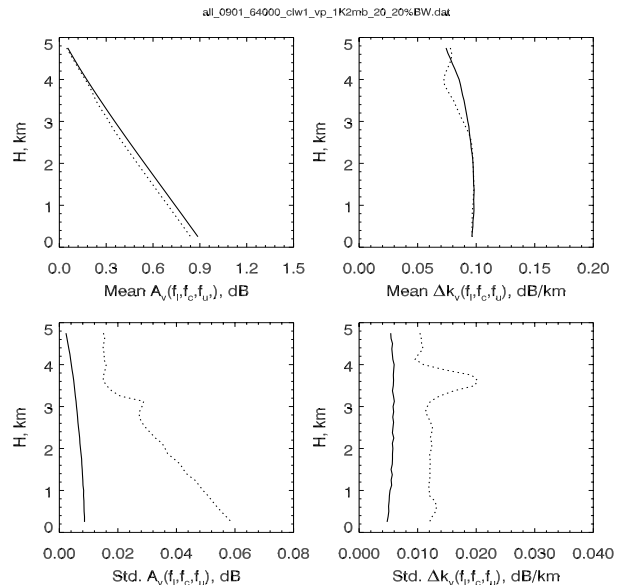


Fig. 5. Top panels show the mean of the differential path absorption and the specific differential absorption of water vapor for the assumed (solid) and retrieved (dotted) values versus height. Bottom panels show the corresponding standard deviation of these quantities.

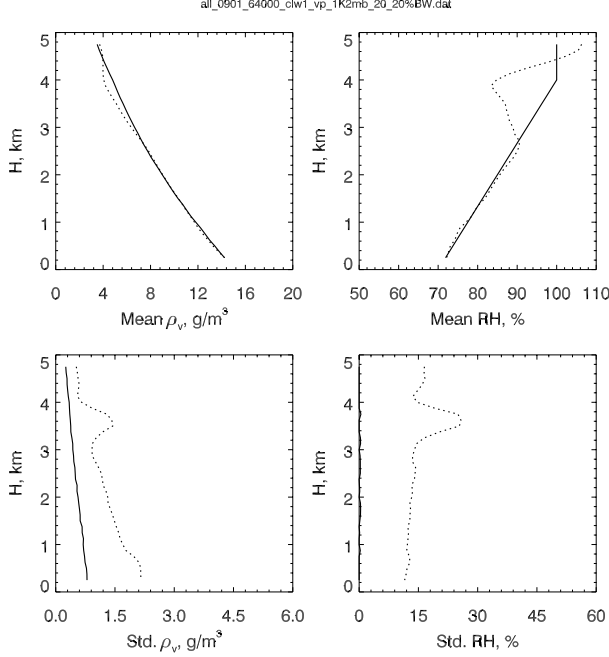


Fig. 6: Top panels show the mean of the water vapor density, ρ_v (g m^{-3}) and relative humidity for the assumed (solid) and retrieved (dotted) values versus height. Bottom panels show the corresponding standard deviation of these quantities. Note that since the ‘true’ temperature and pressure are assumed to vary from profile to profile, the standard deviation in the ‘true’ ρ_v is non-zero. On the other hand, the relative humidity is taken to be constant throughout so that the standard deviation of this quantity is zero.

profiles, the water vapor density and relative humidity are computed. The ‘true’ temperature and pressure profiles are taken to be Gaussian random variables with a mean given by the model profiles with standard deviations of 1 K and 2 millibar, respectively, as derived from 200 soundings in the South China Sea.

The normalized RMS error for water vapor density is computed by:

$$\left[N^{-1} \sum_{i=1}^N \left(\frac{\hat{\rho}_{v,i} - \rho_{v,true}}{\rho_{v,true}} \right)^2 \right]^{1/2} \quad (15)$$

with a similar expression for the relative humidity. Using the results from the simulation, we obtain normalized RMS values of about 15% in the layer from the surface to about 3 km for both the water vapor and relative humidity. Above 3 km, however, the relative error increases to a maximum in the melting layer of about 30%. It is also clear from the top panels of Fig. 6 that estimates of ρ_v and RH are negatively biased in and about the melting layer. If the retrievals are done for an independent sample number of 16,000 rather than 64,000, the relative error in the lowest 3 km increases to

about 20-25%, reaching a maximum error in the melting layer of about 33%.

For the example considered, the fractional bandwidth was taken to be 0.2, with the lower and upper frequencies chosen such that $k_v(f_l) \approx k_v(f_u)$. For the case shown below, in Fig. 7, we have chosen $(f_l, f_c, f_u) = (21.248, 22.235, 26.079)$ GHz, giving a fractional bandwidth of 0.22 and, from (7), $\gamma = 0.1894$. Note that $k_v(f_l) \neq k_v(f_u)$ for this set of frequencies.

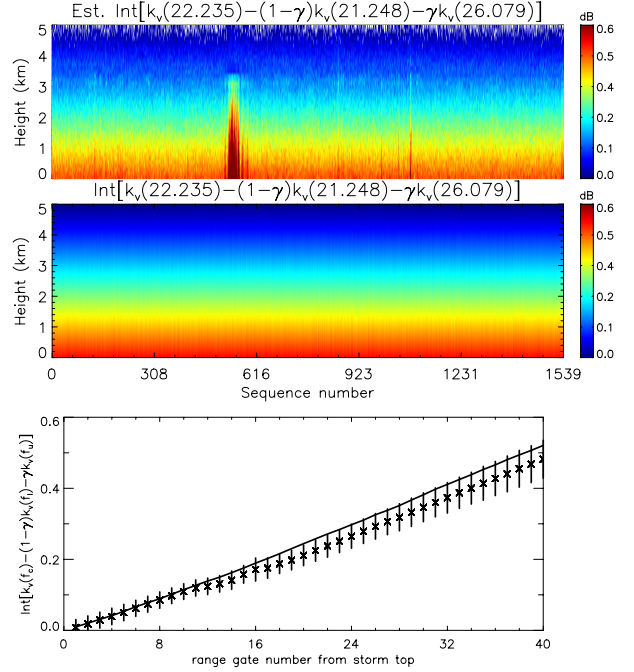


Fig. 7: Same as Fig. 2 but for a different choice of frequencies.

The quantity that we wish to estimate, shown in the center panel of Fig. 7, has a dynamic range of about half that in Fig. 2. Since the sources of error remain about the same as before, it implies that the relative error in the estimate increases by about a factor of 2. Similar increases in the errors in ρ_v and RH are obtained. Another choice that has been considered is:

$(f_l, f_c, f_u) = (20.246, 22.235, 26.079)$ GHz, corresponding to a fractional bandwidth of 0.26 and $\gamma = 0.3154$. We have found that the performance for this set of frequencies is comparable to the first case considered; however, such a large fractional bandwidth is presently not suitable for a differential-frequency implementation.

4. DSD ESTIMATION

In obtaining an estimate involving only the differential water vapor absorption from (4) and (5), the goal was to

eliminate the dependence on attenuation from precipitation and cloud by using the approximation:

$$A_{pc}(f_c, f_l) = \gamma A_{pc}(f_u, f_l) \quad (6)$$

In principle, a similar kind of approximation can be used to obtain a function of A_{pc} independent of the water vapor absorption. In particular, we define β such that:

$$A_v(f_c, f_l) = \beta A_v(f_u, f_l) \quad (16)$$

Unlike γ , which is always positive and less than 1, β is negative when $k_v(f_l) > k_v(f_u)$. Note also that if $k_v(f_l) = k_v(f_u)$ then $A_v(f_u, f_l) = 0$ and β is undefined.

Multiplying (4) by β and subtracting it from (5) yields an expression involving A_{pc} of exactly the same form as (8) and the subsequent equations:

$$2 \int_0^r [k_{pc}(f_c) - (1-\beta)k_{pc}(f_l) - \beta k_{pc}(f_u)] ds = G_m(\beta) - (E_1 + E_2) \quad (17)$$

where

$$G_m(\beta) = \beta \tilde{Z}_m(f_u) + (1-\beta)\tilde{Z}_m(f_l) - \tilde{Z}_m(f_c) \quad (18)$$

$$E_1 = G(\beta) = \beta \tilde{Z}(f_u) + (1-\beta)\tilde{Z}(f_l) - \tilde{Z}(f_c) \quad (19)$$

$$E_2 = A_v(f_c, f_l) - \beta A_v(f_u, f_l) \quad (20)$$

where in (17), $k_{pc} \equiv k_p + k_c$.

For the case shown in Fig. 7, where $(f_l, f_c, f_u) = (21.248, 22.235, 26.079)$ GHz, we find that, near the surface, $\beta = -0.2964$. For the few cases considered with different water vapor density profiles, the values of β near the surface are fairly stable; nevertheless, additional computations are needed to determine its stability over a wider range of conditions.

Using the above value of β , the LHS of (17), which is equal to $A_{pc}(f_c, f_l) - \beta A_{pc}(f_u, f_l)$, and $G_m(\beta), G(\beta)$ from (18) and (19) are shown in Fig. 8. As with the water vapor estimation, $G_m(\beta)$ is used as the estimate while $E_1 = G(\beta)$ and E_2 are error sources. Comparisons of the results in the top and center panels are shown in Fig. 9 as a scatter plot. The results indicate that $G_m(\beta)$ is a reasonably good estimator of

$A_{pc}(f_c, f_l) - \beta A_{pc}(f_u, f_l)$ despite scatter at lower values and a positive bias. If the result can be shown to be valid over a range of water vapor density profiles, it will be useful in solving the dual-wavelength radar equations in that it provides an estimate of path attenuation, a quantity that has been shown to be important for stable retrievals of the parameters of the drop size distribution.

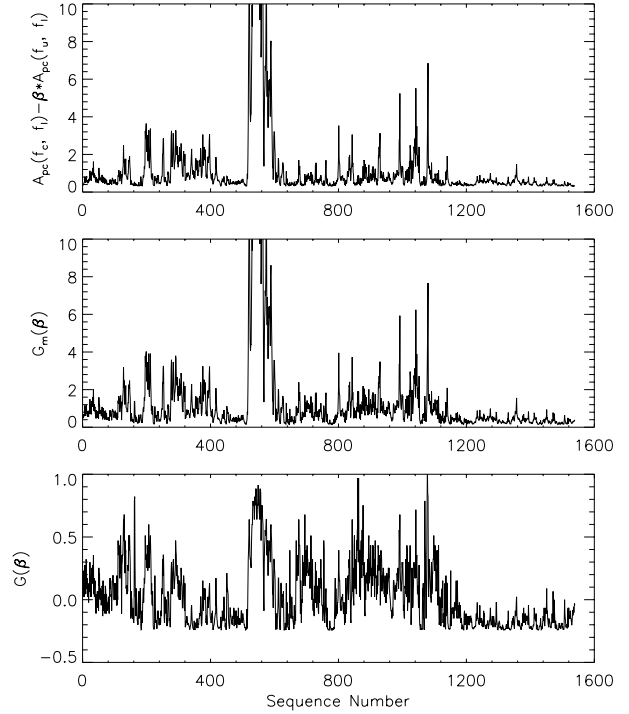


Fig. 8. True (top) and estimated (center) values of a function of the path-integrated attenuation. Bottom: Corresponding sequence of the dominant error term.

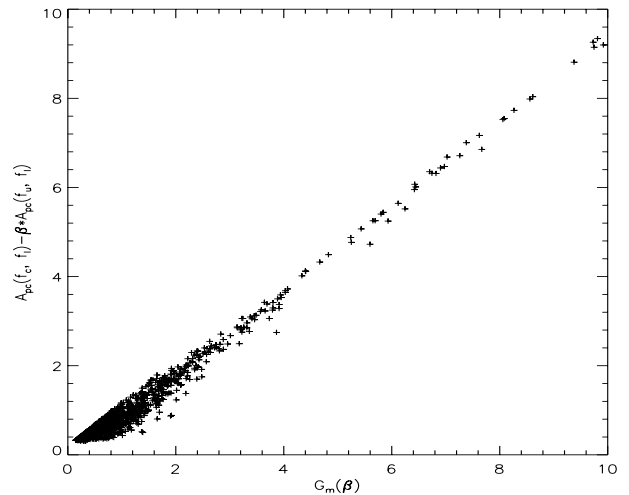


Fig. 9. Scatter plot of the data shown in the top and center panels of Fig. 8.

5. SUMMARY AND CONCLUSIONS

In this paper we have focused on simulations of a water vapor absorption algorithm in rain using radar returns from a three-frequency radar with center frequency at the microwave absorption line center at 22.235 GHz. The results show that retrievals can be made, in principle, for a fractional bandwidth (a ratio of the difference between the higher and lower frequency to the center frequency) of 0.2. However, as the differential water vapor path absorption is only on the order of about 1 dB a very large number of independent samples (16,000 or greater) are needed to make the retrievals reasonably accurate. Moreover, significant biases are seen in the estimates in and about the melting layer. For airborne or spaceborne platforms, pulse compression or whitening methods [Koivunin and Kostinski, 1999; Torres and Zrnic, 2003] would probably be required to achieve this number of independent samples within a few seconds. Also desirable is the use of a single transceiver and antenna to keep the size, weight and cost of the system to a minimum. This requires, in turn, a wide-band power amplifier and antenna with center frequency near 22.235 GHz. Availability of wide-band components and restrictions in frequency allocation may require flexibility in the choice of frequencies. Frequency selections were considered for which the specific absorption for water vapor at the high and low frequencies are unequal. Although the basic method remains applicable, it was shown that the accuracy usually degrades as a consequence of a reduction in the dynamic range of the signal.

While the focus of the paper is on parameters of the water vapor, estimation of path attenuation from precipitation and cloud appears to be possible when the specific absorptions of water vapor at the high and low frequencies are not equal. In fact, the approach appears to be feasible even when the high and low frequency water vapor absorption are nearly the same. This opens the possibility of solving the dual-wavelength equations for the drop size distribution parameters without the need of independent estimates of path attenuation. However, the success of the approach depends on how stable the parameter β is to changes in the water vapor absorption profile. On the other hand, it is worth noting that if accurate estimates of the $A_v(f)$ are derived from the algorithm outlined in section 2, then an accurate determination of β may be obtained directly from the $A_v(f)$ estimates.

Although the method was analyzed only under the assumption that rain is present, a down-looking airborne or spaceborne 3-frequency radar might provide path-integrated estimates of water vapor in the absence of rain by using the surface rather than the rain return [Meneghini et al., 2005]. This appears to be feasible if the frequency dependence of the surface return is known and stable.

ACKNOWLEDGMENTS

We wish to thank Professor Ramesh Srivastava for suggesting the use of multiple frequencies for water vapor estimation. We also wish to thank Dr. Rafael Rincon for use of disdrometer data from Wallops Flight Facility. We thank Professor Chandrasekar for referring us to the paper by Ware et al.

REFERENCES

- Koivunen, A.C. and A.B. Kostinski, 1999: The feasibility of data whitening to improve performance of weather radar. *J. Appl. Meteor.*, **38**, 741-749.
- Liljegren, J.C., 2004: Improved retrievals of temperature and water vapor profiles with a twelve-channel radiometer. Eighth Symposium On Integrated Observing and Assimilation Systems for Atmosphere, Oceans and Land Surface. Amer. Meteor. Soc., 11-15 Jan., Seattle, WA.
- Meneghini, R., L. Liao, and L. Tian, 2005: A feasibility study for simultaneous estimates of water vapor and precipitation parameters using a three-frequency radar. *J. Appl. Meteor.* (in press).
- Tian, L., R.C. Srivastava, G.M. Heymsfield, and L. Li, 2004: Estimation of raindrop-size distribution in stratiform rain from dual-wavelength airborne Doppler radars. Proc. Second TRMM International Science Conference, September 5-10, 2004, Nara, Japan.
- Torres, S.M., and D. S. Zrnić, 2003: Whitening in range to improve weather radar spectral moment estimates. Part I: formulation and simulation. *J. Atmos. Oceanic Technol.*, **20**, 1433-1448.
- Ulaby, F. T., R.K. Moore, and A.K. Fung, 1981: ***Microwave Remote Sensing***. Vol. 1., Addison-Wesley, 456pp.
- Ware, R., D. Cimini, P. Herzegh, F. Marzano, J. Vivekanandan, and E. Westwater, 2004: Ground-based microwave radiometer measurements during precipitation. Eighth Specialist Meeting on Microwave Radiometry. 24-27 Feb., Rome, Italy.
- Waters, J.W., 1976: Absorption and emission of microwave radiation by atmospheric gases, in *Methods of Experimental Physics*, M.L. Meeks, ed., 12, Part B, Radio Astronomy, Academic Press, Section 2.3.
- Yokoyama, T. and H. Tanaka, 1984: Microphysical processes of melting snowflakes detected by two-wavelength radar, *J. Meteor. Soc. Japan*, **62**, 650-666.